FOUNDATIONS
ADVANCES

ISSN 2053-2733

Synchrotron powder diffraction of silicon: high-quality structure factors and electron density

Nanna Wahlberg,[a] Niels Bindzus,[a] Lasse Bjerg,[a] Jacob Becker,[a] Ann-Christin Dippel[a,b] and Bo Brummerstedt Iversen[a]*

[a]Department of Chemistry, Aarhus University, Langelandsgade 140, Aarhus 8000, Denmark, and [b]Deutsches Elektronen-Synchrotron DESY, Notkestrasse 85, Hamburg D-22607, Germany. *Correspondence e-mail: bo@chem.au.dk

Received 30 June 2015
Accepted 30 September 2015

Edited by W. F. Kuhs, Georg-August University Göttingen, Germany

Keywords: synchrotron powder X-ray diffraction; charge density; core polarization; structure factors; silicon.

Supporting information: this article has supporting information at journals.iucr.org/a

Crystalline silicon is an ideal compound to test the current state of experimental structure factors and corresponding electron densities. High-quality structure factors have been measured on crystalline silicon with synchrotron powder X-ray diffraction. They are in excellent agreement with benchmark *Pendellösung* data having comparable accuracy and precision, but acquired in far less time and to a much higher resolution ($\sin\theta/\lambda < 1.7$ Å^{-1}). The extended data range permits an experimental modelling of not only the valence electron density but also the core deformation in silicon, establishing an increase of the core density upon bond formation in crystalline silicon. Furthermore, a physically sound procedure for evaluating the standard deviation of powder-derived structure factors has been applied. Sampling statistics inherently account for contributions from photon counts as well as the limited number of diffracting particles, where especially the latter are particularly difficult to handle.

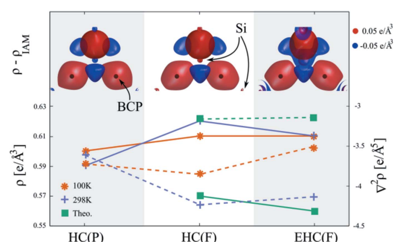

© 2016 International Union of Crystallography

1. Introduction

Synchrotron powder X-ray diffraction (SPXRD) has in recent years evolved into an attractive technique for probing the electron density (ED) of extended inorganic materials (Jørgensen *et al.*, 2014). At the cost of collapsing the three-dimensional reciprocal space into one, SPXRD largely resolves the intrinsic challenges tied to this class of materials by delivering data with negligible extinction and reduced absorption. The present study exploits such qualities to determine benchmark structure factors on crystalline silicon (cSi), which for the low-temperature case extend to an exceptionally high resolution. With its monatomic structure, low atomic number and well studied electronic properties, cSi presents a point of reference for evaluating novel and existing *ab initio* methods (Pisani *et al.*, 1992; Zuo *et al.*, 1997; Lu & Zunger, 1992). Thus, it is of general interest to determine the experimental data of cSi at the best possible level.

In X-ray diffraction structure factors are determined, which are defined as the Fourier coefficients of the ED,

$$F_{\mathbf{H}} = \int \rho(\mathbf{r}) \cdot T \exp(2\pi i \mathbf{H} \cdot \mathbf{r})\, \mathrm{d}\mathbf{r}, \qquad (1)$$

where $\mathbf{H} = h\mathbf{a}^* + k\mathbf{b}^* + l\mathbf{c}^*$ is the reciprocal-lattice vector, T is a probability function that accounts for thermal motion, and $\rho(\mathbf{r})$ is the ED at the point $\mathbf{r}$. Within the kinematic framework, the incoming photons are assumed to scatter only once and a simple relationship connects the structure factors to the measured intensities, $I_{hkl} \propto |F_{hkl}|^2$ (Giacovazzo, 2002). To avoid multiple scattering events and insufficient correction models (Yamamoto *et al.*, 1996), accurate structure factors of cSi have in the past been measured by the dynamical *Pendellösung* method (Kato, 1988). In fact, its disposition

towards perfect crystallinity has made cSi one of the main compounds for this ambitious and extremely time-demanding technique (Teworte & Bonse, 1984; Saka & Kato, 1986; Aldred & Hart, 1973). Among the reported data, the averaged structure factors corrected for anomalous dispersion are regarded as superior and are herein referred to as $F_{\rm PEND}$ (Deutsch & Hart, 1988; Cummings & Hart, 1988).

Re-entering the kinematic regime, Nishibori *et al.* convincingly demonstrated that an accuracy comparable to that of the *Pendellösung* technique is achievable by state-of-the-art SPXRD (Nishibori *et al.*, 2007). In the current study we improve the SPXRD experiment by conducting it in vacuum and with shorter X-ray wavelength, thereby improving the resolution and signal-to-background. In addition to a good determination of the high-intensity reflections, the high-order low-intensity reflections are measured more accurately, since these in particular are affected by the noise from air scattering.

An observation is meaningless if no uncertainty is assigned. This bold statement clearly stresses the importance of knowing not only the magnitude of a structure factor, $|F|$, but also its uncertainty, σ_F. Crystallographic structure factors are used to refine a model by least-squares refinement, where σ_F defines the weights (Giacovazzo, 2002). Thus, wrong estimates of the uncertainty may at best result in wrong estimates of the model parameter uncertainties, and at worst in an incorrect model. When determined by SPXRD, the σ_F's are propagated from the uncertainties of the pattern intensities. Consequently, it is of great importance to determine the pattern uncertainties correctly. Traditionally, only Poisson statistics have been applied which effectively ignore the contribution from the limited number of diffracting particles in the sample (Ida, 2011; Ida & Izumi, 2011; Alexander *et al.*, 1948; De Wolff, 1959).

This paper demonstrates how excellent SPXRD of high resolution with a good uncertainty estimate can be used in advanced modelling of the ED. Indeed, prior studies on diamond and cubic boron nitride have demonstrated that the core region ED can be determined from SPXRD data (Bindzus *et al.*, 2014; Wahlberg *et al.*, 2015). Being isostructural with diamond, silicon represents a case where the core ED composes the largest contribution to the structure factors even at low order (four valence electrons as opposed to ten core electrons). As shown below, the scattering magnitude and high data resolution even allow us to subdivide the core ED into two separate ED functions, largely representing the *K* and *L* shells, producing a model of unseen quality and complexity.

2. Experimental details

2.1. Synchrotron powder X-ray diffraction data

Diffraction data at 100 K and 298 K were collected at the PETRA III beamline P02.1 using high-energy X-rays (60 keV, λ = 0.2072 Å). The silicon sample (NIST 640d, median particle diameter 4.1 µm) packed in a 0.2 mm glass capillary was continuously rotated during data collection to improve the particle statistics. To ensure a better determination of the high-order reflections, the diffraction experiment was conducted in vacuum, thereby minimizing background scattering from air (Straasø *et al.*, 2013). Data were obtained at room temperature (RT) and at 100 K by cooling the sample with a jet of helium at liquid-nitrogen temperature (Dippel *et al.*, 2014). Fractions of the Debye–Scherrer cones were collected on image plates, which after digitalization (GE Typhoon FLA 700 scanner) were integrated to a one-dimensional diffraction pattern (Fig. 1).

2.2. Computational details

The theoretical electronic structure was determined in the experimental geometry employing density functional theory (DFT) methods incorporated in the *WIEN2k* software package (Blaha *et al.*, 2008). Calculations were performed

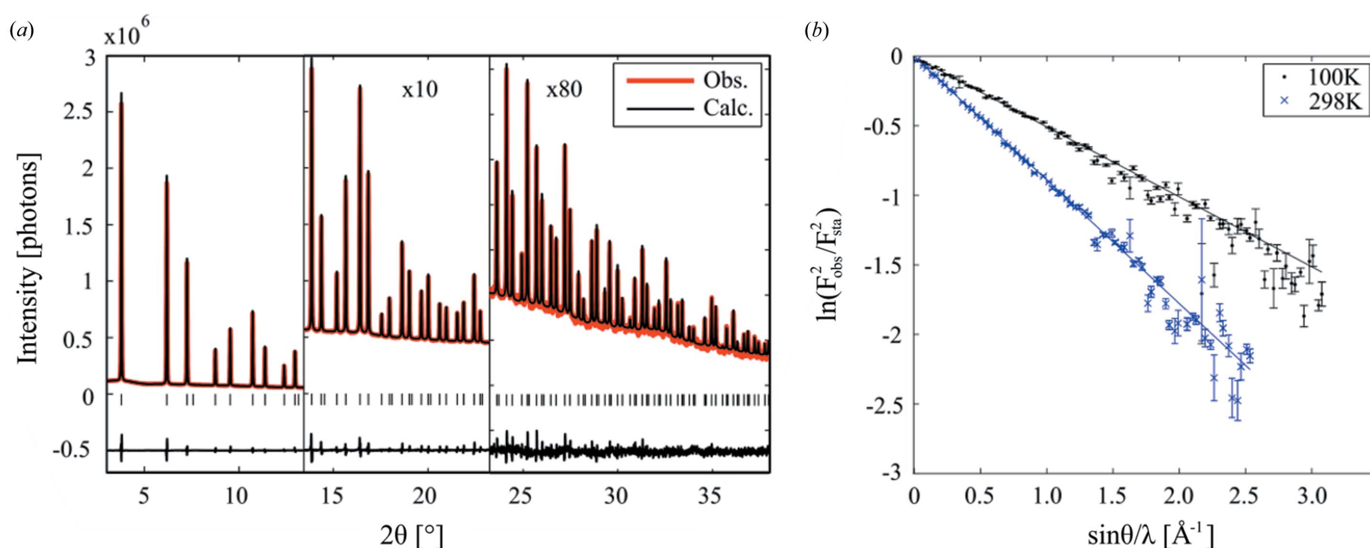

Figure 1
(*a*) Observed and calculated diffraction pattern at 298 K. (*b*) Wilson plot of the observed structure factors of the third iteration against the calculated static structure factors.

using the PBE functional (Perdew *et al.*, 1996) on a 46 × 46 × 46 k-grid with RK_{max} = 10. The ED within the atomic spheres was expanded to include spherical harmonics up to L = 10. Static structure factors were obtained by Fourier transformation of the theoretical ED.

3. Electron-density models

The simplest ED model is the conventional independent-atom model (IAM), where the total ED is assumed to be a superposition of isolated ground-state atoms. An atom-centred multipole model has the flexibility to describe atomic interactions such as covalent bonding and charge transfer (Stewart, 1976). In the standard Hansen–Coppens multipole formalism (HC), the total ED is constructed from a superposition of pseudo-atoms, each containing an inert core in addition to an adjustable spherical and aspherical valence density (Hansen & Coppens, 1978):

$$\rho_{\rm at}(\mathbf{r}) = P_{\rm c}\rho_{\rm c}(r) + P_{\rm v}\kappa^3\rho_{\rm v}(\kappa r) + \sum_{l=0}^{l_{\max}} \kappa'^3 R_l(\kappa' r) \sum_{m=0}^{l} P_{lm\pm} d_{lm\pm}(\theta,\varphi), \qquad (2)$$

where $P_{\rm c}$ and $P_{\rm v}$ denote the electronic population of the spherical components, whereas the aspherical part is modelled by real spherical harmonics, $d_{lm\pm}$, with individual population parameters, $P_{lm\pm}$. Radial expansion and contraction of the atomic ED are regulated by κ and κ'. The tetrahedral site symmetry of the silicon atom restricts all other populations than P_{32-}, P_{40} and P_{44+} to zero when expanding to fourth order, where the allowed hexadecapoles are linearly dependent.

The extended Hansen–Coppens model (EHC) abandons the basic assumption of an inert core by parameterizing the inner shells of the atom (Fischer *et al.*, 2011). The HC model is expanded by adding functions similar to the spherical and aspherical density functions of the valence ED to the inner ED:

$$\rho_{\rm at}(\mathbf{r}) = \sum_{n=1}^{N}\left[P_n\kappa_n^3\rho_n(\kappa_n r) + \sum_{l=0}^{l_{\max}} \kappa_n'^3 R_{l,n}(\kappa_n' r) \sum_{m=0}^{l} P_{nlm\pm} d_{lm\pm}(\theta,\varphi)\right], \qquad (3)$$

where N is the number of shells in the atom 'at'. In the current analysis of silicon, it was sufficient to allow for spherical deformation of the inner shells, thereby introducing four extra parameters (we add a K and L shell: P_K, P_L, κ_K and κ_L).

3.1. Thermal deconvolution

A fundamental step in ED studies is the deconvolution of thermal motion. For monatomic compounds, a Wilson plot is a reliable method for estimating the isotropic atomic displacement parameter (ADP) (Wilson, 1942):

$$\ln\left(\frac{F_{\rm obs}^2}{F_{\rm sta}^2}\right) = \ln(k) - 16\pi^2 U_{\rm iso}\frac{\sin^2\theta}{\lambda^2}. \qquad (4)$$

The cubic site symmetry of Si restricts the atomic displacement to spherical within the harmonic approximation, and a complete set of static structure factors, $F_{\rm sta}$, is calculated by DFT. The slope of equation (4) is proportional to the isotropic ADP, $U_{\rm iso}$, while the vertical intersection represents the scale factor (k) of the experimental data.

4. Structure-factor extraction

Since a powder diffraction experiment measures a one-dimensional projection of the complete scattering pattern, the recovery of the structure factors, $F_{\rm obs}$, constitutes a key challenge. The cubic symmetry and short unit-cell length of cSi [$Fd\overline{3}m$, a = 5.43123 (8) Å], however, minimize model effects by a recognizable background profile and eliminating virtually all peak overlap at low order.

4.1. Estimation of uncertainty

An important and often neglected aspect in the analysis of powder patterns is the procedure for estimating standard deviations of the structure factors, σ_F. Contrary to the empirical schemes implemented in common refinement programs (Bindzus & Iversen, 2012), we propose a simple and physically founded procedure that exploits the available information in an area detector. Since the exposed part of the applied image-plate detector is 400 pixels wide, it provides the equivalent number of independent measurements for every point in the diffractogram. Alternatively to estimating the uncertainties in the diffraction pattern from Poisson statistics, possibly even combined with more advanced particle statistics (Ida, 2011; Ida & Izumi, 2011), we suggest simple sample statistics. We assume that every point along the integration arc is an independent observation and from this data set determine the standard deviation:

$$\sigma = \left[\frac{\sum_{x=1}^{n}\left(I_x - \langle I_{2\theta}\rangle\right)^2}{(n-1)}\right]^{1/2}, \qquad (5)$$

where I_x is the intensity at the point x on the integration path and $\langle I_{2\theta}\rangle$ is the average intensity. The standard deviation of the mean thereby becomes

$$\sigma\left(\langle I_{2\theta}\rangle\right) = \frac{\sigma}{n^{1/2}}. \qquad (6)$$

However, since we use the sum and not the mean of the intensity, the uncertainty is rescaled according to propagation of uncertainties:

$$\sigma\left(y_{2\theta}\right) = \sigma\left(\langle I_{2\theta}\rangle\right) \times n, \qquad (7)$$

since

$$y_{2\theta} = \sum_{x=1}^{n} I_{2\theta,x} = \langle I_{2\theta}\rangle \times n. \qquad (8)$$

The uncertainties of the pattern points are converted by error propagation as given in the supporting information. Notably, this simple procedure includes all sources of error, abandoning a simplistic belief in counting statistics as the sole contributor.

Table 1
Rietveld refinement results.

Fixed parameters are listed without uncertainties. 'Free' is the initial refinement where the ADP is freely refined, w1 and w2 are the first and second iterations where the ADPs are determined from the Wilson plot. GOF is goodness of fit.

	Free (100 K)	w1 (100 K)	w2 (100 K)	Free (298 K)	w1 (298 K)	w2 (298 K)
R/wR	1.93/0.73	1.74/0.70	1.72/0.70	1.30/0.59	1.28/0.58	1.29/0.59
R_p/wR_p	1.08/1.13	1.08/1.13	1.08/1.13	1.12/0.90	1.12/0.90	1.12/0.90
GOF	3.69	3.69	3.69	2.62	2.62	2.62
Scale	0.9007 (5)	0.9020 (4)	0.9022 (4)	0.9644 (7)	0.9660 (4)	0.9662 (4)
Shift ($10^{-2\circ}$)				0.074 (3)	0.074 (3)	0.074 (3)
Asym	−0.021 (1)	−0.020 (1)	−0.020 (1)	−0.032 (1)	−0.032 (1)	−0.032 (1)
a (Å)	5.430657 (9)	5.430657 (9)	5.430657 (9)	5.431230	5.431230	5.431230
GW	2.233 (7)	2.237 (7)	2.238 (7)	2.329 (7)	2.333 (6)	2.333 (6)
LX	0.799 (6)	0.803 (5)	0.804 (6)	0.694 (5)	0.695 (5)	0.696 (5)
LY	3.95 (7)	3.85 (7)	3.84 (7)	2.43 (6)	2.37 (6)	2.37 (6)
$U_{iso} \times 10^{-4}$ (Å^2)	31.1 (2)	31.72	31.81	55.5 (2)	56.12	56.20
K	0.98 (1)	0.98 (1)	0.98 (1)	0.97 (1)	0.98 (1)	0.98 (1)
κ'	1.29 (4)	1.32 (4)	1.33 (4)	1.16 (4)	1.20 (4)	1.21 (4)
P_{32-}	0.36 (3)	0.35 (3)	0.35 (3)	0.37 (3)	0.36 (3)	0.36 (3)
P_{40}	−0.16 (4)	−0.15 (3)	−0.15 (3)	−0.26 (7)	−0.22 (5)	−0.2 1(5)
Wilson plot						
U_{iso}/scale	31.72 (18)/ 0.9974 (16)	31.81 (18)/ 0.9943 (15)	31.83 (18)/ 0.9936 (15)	56.12 (42)/ 1.0007 (16)	56.20 (43)/ 1.0026 (16)	56.20 (43)/ 1.0026 (16)

4.2. Pattern fitting

The patterns are fitted with the model-dependent Rietveld refinement method in *Jana2006* (Rietveld, 1969; Petříček *et al.*, 2006). In cSi only complete peak overlap occurs caused by two more reflections with reciprocal-lattice vectors of equal lengths (first incidence at $\sin\theta/\lambda$ = 0.66 Å^{-1}). In the case of overlap the contribution of each reflection to the measured peak is determined from the ratio between the corresponding model reflections. Thus, the model used in the extraction may affect the magnitude of the extracted structure factors.

In the direct pattern fitting the HC model was used to represent the ED, and the thermal motion was deconvoluted by a Wilson plot. However, the model dependency of the Rietveld method requires an iterative procedure: the U_{iso} determined from the extracted structure factors is used in a subsequent Rietveld refinement. This is repeated until the ADPs are identical within the estimated error (Table 1, Fig. 1*b*).

The peak shape was satisfactorily reproduced by two Lorentzian functions (LY and LX) and a Gaussian function (GW). Though the two-dimensional data were integrated along an arc, asymmetry was still present in the peaks. This was readily accounted for by Simpson's asymmetry correction (asym). The background was determined by linear interpolation between 60 points. The cell edge length was not refined at room temperature (NIST standard), instead a shift parameter was included. All parameters are listed in Table 1.

4.3. Structure-factor quality

Comparison with F_{PEND} demonstrates that state-of-the-art SPXRD measures structure factors with comparable accuracy (Fig. 2*a*). Agreement factors, $R = \sum ||F_{obs}| - |F_{PEND}|| / \sum |F_{obs}|$, of 0.57% at 100 K and 0.25% at RT verify the good agreement between the different measurements. The better correspondence with the RT data reflects a similar acquisition temperature compared with the *Pendellösung* data, as anharmonicity and second-order effects like thermal diffuse scattering (TDS) persist in the experimental structure factors deconvoluted with an isotropic ADP.

The relative uncertainty of the 100 K structure factors is shown in Fig. 2(*b*) and compared to the corresponding case of pure Poisson statistics, where the error of the powder pattern is assumed to be $\sigma_y = y^{1/2}$. Deviations are restricted to the low-order region and represent dominant contributions from particle statistics (Alexander *et al.*, 1948; De Wolff, 1959). This observation agrees with diamond data collected under similar conditions as the error from a limited number of particles was demonstrated to dominate at $\sin\theta/\lambda < 1$ Å^{-1} (Straasø *et al.*, 2014). Without resorting to comprehensive and approximate models (Ida, 2011), the proposed procedure by its very definition includes such complex effects.

Moreover, the similarity to the significance of F_{PEND} establishes that also the precision of SPXRD parallels the *Pendellösung* technique (Fig. 2*b*). Such a performance is even more remarkable when it is taken into account that the data extend to a far higher resolution and were acquired in merely 50 min. This underlines that SPXRD indeed has reached a stage where for extended inorganic materials it can compete with and even surpass techniques based on single crystals.

Though weak, the symmetry-forbidden 222 reflection has been detected for cSi in several cases (Nishibori *et al.*, 2007; Fujimoto, 1974; Roberto *et al.*, 1974; Roberto & Batterman, 1970; Alkire *et al.*, 1982). Its occurrence is due to the presence of an acentric component in the structure factor, which primarily arises from the covalent bonding (Roberto & Batterman, 1970; Roberto *et al.*, 1974; Keating *et al.*, 1971; Dawson, 1967). In contrast, higher-order reflections of the $h + k + l = 4n + 2$ group exhibit significant anharmonic features. These are presently too weak to be observed, prohibiting an unambiguous modelling of anharmonic ADPs and the corresponding structure-factor correction (Trucano &

Batterman, 1972). The anharmonic contribution to the thermal displacement can be modelled by refining population parameters of the probability density functions in the Gram–Charlier expansion (Johnson & Levy, 1974). However, refining the symmetry-allowed third-order population improves neither the pattern fit nor the Bragg residuals regardless of temperature (see Table S1). On a statistical basis the data are therefore unsupportive of the existence of a significant anharmonic contribution to the ADPs. On the other hand, the resulting probability density functions are in close agreement with expectations of an increased probability in the opposite direction of the covalent bond (see Fig. S2). The electron-density model is not significantly changed upon inclusion of anharmonic parameters and in light of the ambiguity in the ADP modelling we proceed with the harmonic ADPs. At 100 K this is a reasonable approximation, while small errors inevitably are introduced at RT (Spackman, 1986; Lu *et al.*, 1993; Flensburg & Stewart, 1999). The analysis of our SPXRD data determines F_{222} to be 1.73 (5) and 1.67 (5) at 298 and 100 K, respectively. When determined by kinematic γ-ray diffraction at RT and neglecting multiple scattering effects, F_{222} = 1.456 (8) (Alkire *et al.*, 1982). Other measurements are predominantly in closer agreement with the γ-ray diffraction result (Price *et al.*, 1978). Thus, the F_{222} determined here are probably exaggerated by 0.1–0.2, but within what is acceptable for a kinematic X-ray experiment. Moreover, its extraction process is prone to errors as its low intensity renders it sensitive to the background modelling. Other sources of error might be uncorrected phenomena such as the *Umweganregung* effects (Alkire *et al.*, 1982; Nishibori *et al.*, 2007; Fujimoto, 1974).

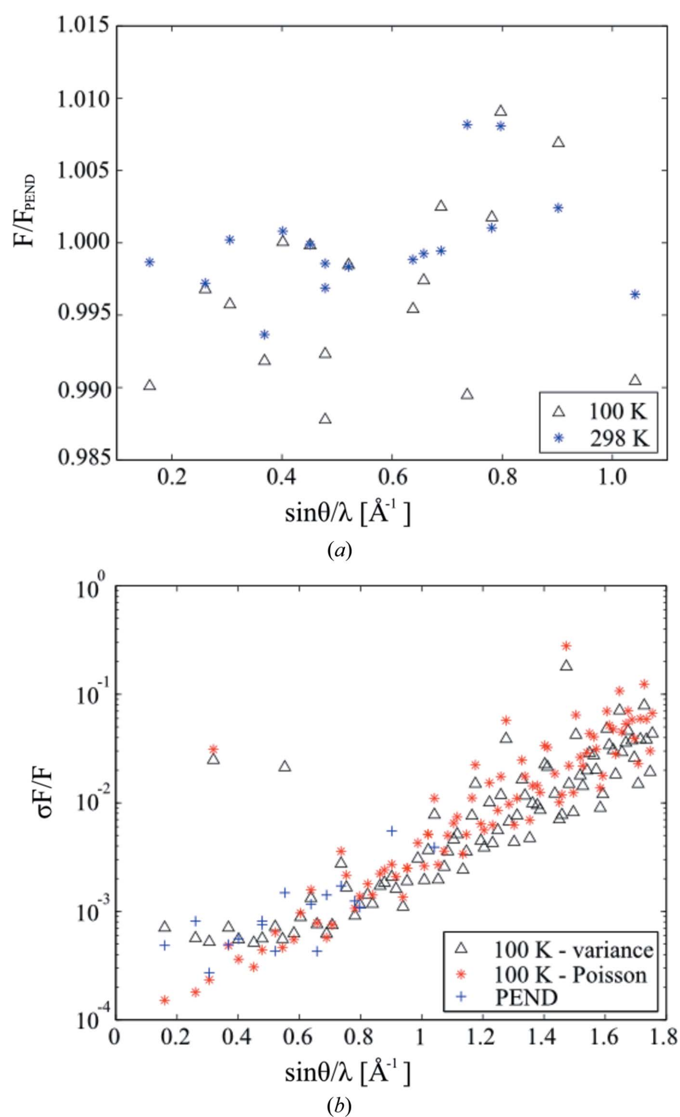

Figure 2
(*a*) Comparison of the ADP-corrected extracted and *Pendellösung* structure factors, corrected for nuclei scattering. (*b*) The significance of the three different data sets on cSi.

5. Electron-density models

To enhance the ED sensitivity of the data, the extracted structure factors are subjected to extensive post-Rietveld modelling, HC(F) and EHC(F). In addition to enhancing the structural sensitivity, this approach reduces correlation as the comprehensive modelling of the diffraction pattern is eliminated. Fig. 4 displays the resulting residual densities in the crystal plane of the Si—Si bond chain for the HC model fitted aginst pattern [HC(P)] and the post-Rietveld models where the data are cut off at $\sin\theta/\lambda$ = 1 $Å^{-1}$ (the full resolution residual maps are shown in Figs. S3 and S4).

In the standard multipole refinements, HC(P) and HC(F), notable features persist in the residual density (Figs. 4*a*, 4*b*, 4*d* and 4*e*). The covalent Si—Si bonding is satisfactorily described, whereas the discrepancies in the innermost region of the Si atoms imply a significant perturbation of the core density, in particular for the 100 K data. It has been a recurring topic of discussion whether such subtle deformations are truly measurable; nevertheless, a recent benchmark study on diamond clarified that it is experimentally feasible (Bentley & Stewart, 1974; Batke & Eickerling, 2013; Fischer *et al.*, 2011; Bindzus *et al.*, 2014). In preceding investigations of cSi, the *L* shell was found to expand (Spackman, 1986; Deutsch, 1992; Lu *et al.*, 1993). Besides a change in the static ED, an independent

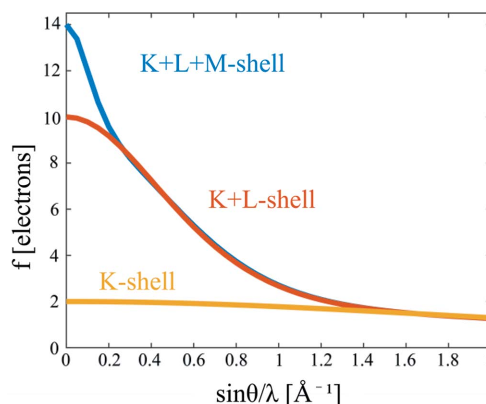

Figure 3
The shell contribution to the atomic Si form factor.

ADP for the inner shell was justified by two distinguishable slopes in the Wilson plot (Deutsch & Hart, 1988; Deutsch, 1992). In the current case, however, no clear evidence exists for such a second ADP (Fig. 1*b*). The 298 K deviations from a straight line in the high-order regime are a consequence of the higher uncertainty in the intensity determination of these reflections. To avoid a high contribution of noise in the model, we cut the 298 K data at 1.3 Å^{-1} ($\sin^2\theta/\lambda^2$ = 1.69 Å^{-1}).

In the present analysis, the lower resolution at RT only allows for the modelling of the *L* shell, while both of the inner shells are probed at 100 K, see Fig. 3. Although the enforced partitioning of the electron density is inspired by Bohr's atomic model, it must be stressed that they are not equivalent; elastic scattering only probes the total density. Moreover, contrary to results from quantum chemistry, the valence ED is represented by nodeless radial functions in the multipole formalism, $R_l(\kappa' r)$ in equation (2).

The EHC model consistently results in near-perfect core fits (Figs. 4*c*, 4*f* and Table 2). At first glance, the 100 K and RT model seem to disagree on the character of the core ED deformation as P_L and κ_L show opposite trends (Table 2). The combined effect of these parameters, however, in both cases tells the story of a decrease in ED in the volume dominated by the *L* shell. At 100 K it was possible to refine the innermost ED parameters, which support the depletion of the core ED by a radial expansion, κ_K = 0.9482 (8). This is in contrast to the strong positive ED feature in the residual map of the HC(F) model at 100 K. This distinct feature is modelled by an increase and contraction of the valence ED function which has finally a contribution in the core region. In addition to improved agreement with the observed structure factors, the EHC model is supported by theory. The values and overall behaviour of the refined core parameter values compare well with what Fischer *et al.* found when refining against theoretical structure factors (Table 2) (Fischer *et al.*, 2011). At both temperatures, the aspherical valence ED is more contracted compared to theory. The spherical valence ED expands at RT in agreement with the theoretical model and in contrast to the minor contraction observed for the 100 K model. We believe this difference arises from the change in unit-cell sizes: RT and

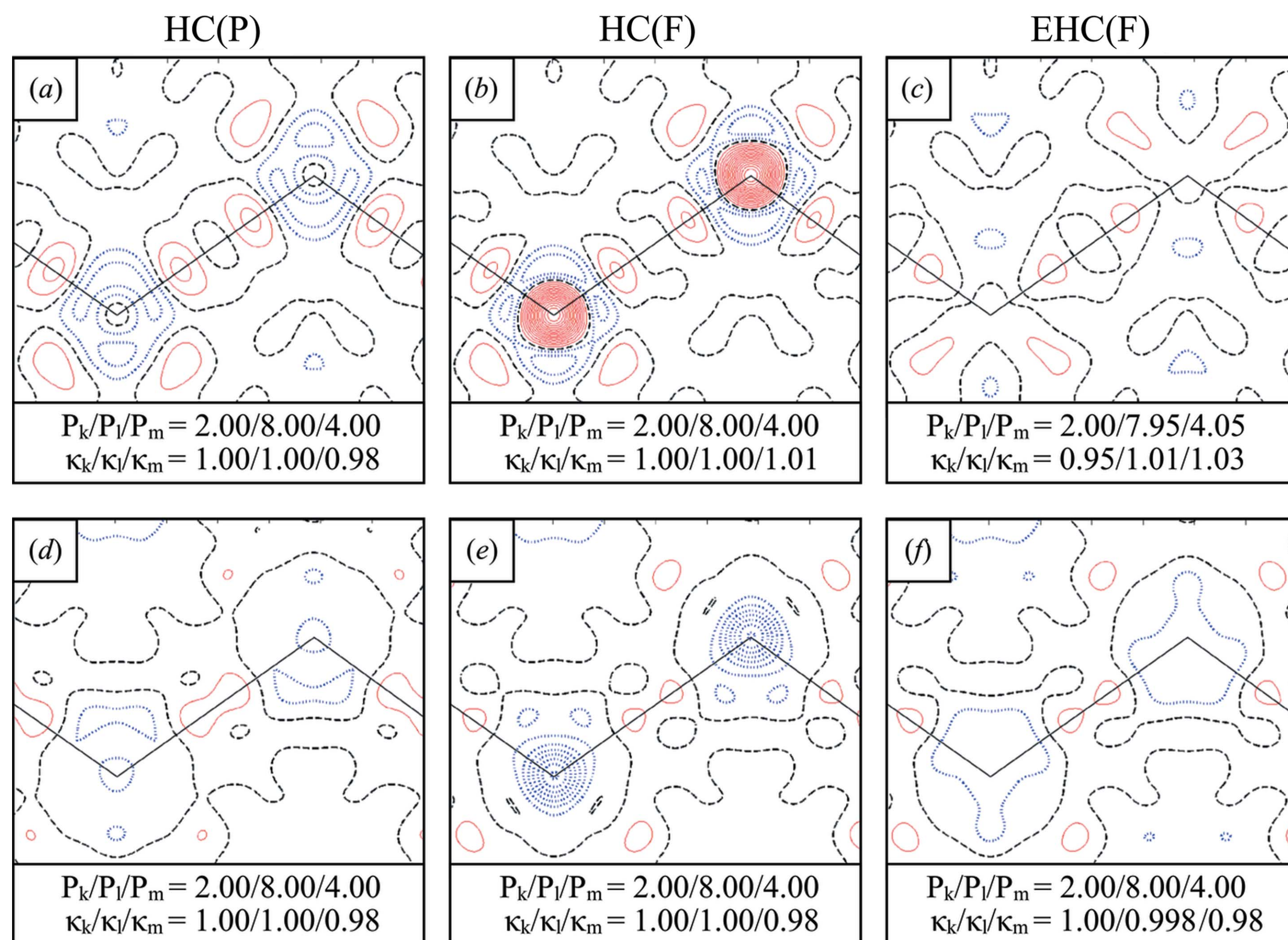

Figure 4
Residual density maps in the (110) crystal plane based on all reflections below $\sin\theta/\lambda$ = 1 Å^{-1}. (*a*)–(*c*) 100 K and (*d*)–(*f*) 298 K. Three multipolar refinements of increasing quality: (*a*), (*d*) HC(P); (*b*), (*e*) HC(F) and (*c*), (*d*) EHC(F). Positive (solid red), negative (dotted blue) and zero density (dashed black). Contour levels drawn at 0.05 e Å^{-3}. For all maps, the error is determined by Fourier transform to be 0.02 e Å^{-3}.

Table 2
Post-Rietveld refinement of the experimental structure factors.

The estimated standard deviations of the constrained parameters are given. Fixed parameters are listed without uncertainties.

	100 K HC	100 K EHC	298 K HC	298 K EHC	Theory†
R/wR	1.42/0.76	1.19/0.48	0.60/0.54	0.57/0.49	0.05
Cut-off (Å^{-1})	1.7	1.7	1.3	1.3	1.8
GOF	4.76	3.03	3.52	3.22	NA
Scale	0.9936	0.9936	1.0026	1.0026	1.0
U_{iso}	31.83	31.83	56.20	56.20	0.0
P_M‡	4.00	4.05 (1)	4.00	4.00	4.055
κ_M	1.01 (1)	1.029 (8)	0.98 (2)	0.98 (2)	0.979
κ'_M	1.35 (6)	1.42 (4)	1.23 (5)	1.24 (4)	1.002
P_{32-}	0.36 (4)	0.33 (2)	0.40 (4)	0.39 (4)	0.424
P_{40}	−0.14 (4)	−0.12 (2)	−0.22 (6)	−0.21 (5)	-0.201
P_L‡	8.00	7.95 (1)	8.00	8.000 (2)	7.978
κ_L	1.00	1.013 (1)	1.00	0.998 (6)	1.0085
P_K‡	2.00	2.000	2.00	2.00	1.966
κ_K	1.00	0.9482 (8)	1.00	1.00	1.023

† 300 K geometry (Fischer *et al.*, 2011). ‡ The total number of electrons is $14 = P_k + P_l + P_m$.

theory have the same unit-cell length, whereas the 100 K is contracted.

Combining the contributions from all the 'shells', the 100 K model reveals an increase while the RT model suggests a decrease in the core ED. The *L*-shell expansion proposed by Spackman was based on the *Pendellösung* data collected at RT, implying that this ED feature is caused by systematic errors such as limited resolution and uncorrected TDS. The increase of the core ED of the 100 K model is in agreement with the related diamond system (Bindzus *et al.*, 2014). The increase of the core ED may be seen as a consequence of covalent bonding: the valence density is relocated into covalent bonds, reducing the electronic shielding of the nuclei for the inner electrons.

The impact of the various multipole models is gauged from the local properties of the Si—Si bond, Fig. 5 (Gatti, 2005). It is apparent that the choice of model only to a minor degree influences the total ED at the bond critical point, merely varying between 0.59 and 0.62 e Å^{-3} in excellent accord with reported values of 0.58 to 0.69 e Å^{-3} (Spackman, 1986; Scheringer, 1980; Yang & Coppens, 1974; Abramov & Okamura, 1997). The significant spread in the Laplacian, however, establishes a clear correlation between model quality and the derivatives of the ED. In consequence, it may be essential to account for core deformation in the evaluation of properties such as the source function, inner moments and interaction energies (Bader & Gatti, 1998; Coppens, 1997). Due to the high correlation between model parameters, this conclusion might extend to evaluations that directly incorporate the multipole parameters.

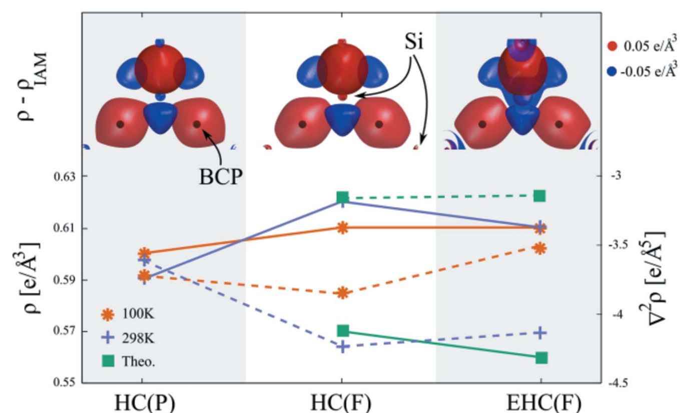

Figure 5
ED (solid lines) and Laplacian (dashed lines) at the bond critical point (BCP) of the HC(P), HC(F) and EHC(F) models. The top panel shows the deformation three-dimensional EDs, $\rho - \rho_{\rm IAM}$, of the 100 K models.

6. Conclusion

In the current study, we have demonstrated that high-quality structure factors comparable in both precision and accuracy to *Pendellösung* data can be obtained by SPXRD for simple high-symmetry compounds. By determining the uncertainty in the diffraction pattern from the variance in the integration process a physically meaningful result is obtained. The uncertainty of the low-order reflection determined by variance is higher than when determined by Poisson statistics, and thereby accounts for the contribution from the limited number of diffraction particles.

The high resolution and well estimated uncertainties permit a detailed modelling of the ED. The higher intensity at high order and low contribution of unmodelled physical phenomena such as TDS and anharmonicity at 100 K allow an explicit fitting of the inner atom ED. The core ED increases compared to the IAM and HC models, which may result from decreased shielding when the valence density is redistributed into covalent bonds. The effect of an explicit core modelling on the local properties of the Si—Si bond is minor; however, the Laplacian is somewhat affected. A complete modelling of the ED may therefore become important when deriving properties based on high-order derivatives.

Acknowledgements

We thank Professor Dr Takashi Ida for pointing out the possibility of determining the σ of a data point based on the numerous observations on a two-dimensional detector. In addition, we would like to thank Dr Vaclav Petříček for detailed documentation on the theoretical foundation of *Jana2006*. We gratefully acknowledge DESY, a member of the Helmholtz Association (HGF), for beam time granted at PETRA III and the Carlsberg Foundation for funding the all-in-vacuum diffractometer. The work was supported by the Danish National Research Foundation (Center for Materials Crystallography, DNRF93) and the Danish Research Council for Nature and Universe (Danscatt).

References

Abramov, Yu. A. & Okamura, F. P. (1997). *Acta Cryst.* A**53**, 187–198.
Aldred, P. J. E. & Hart, M. (1973). *Proc. R. Soc. A Math. Phys. Eng. Sci.* **332**, 223–238.

Alexander, L., Klug, H. P. & Kummer, E. (1948). *J. Appl. Phys.* **19**, 742–753.

Alkire, R. W., Yelon, W. B. & Schneider, J. R. (1982). *Phys. Rev. B*, **26**, 3097–3104.

Bader, R. F. W. & Gatti, C. (1998). *Chem. Phys. Lett.* **287**, 233–238.

Batke, K. & Eickerling, G. (2013). *J. Phys. Chem. A*, **117**, 11566–11579.

Bentley, J. & Stewart, R. F. (1974). *Acta Cryst.* A**30**, 60–67.

Bindzus, N. & Iversen, B. B. (2012). *Acta Cryst.* A**68**, 750–762.

Bindzus, N., Straasø, T., Wahlberg, N., Becker, J., Bjerg, L., Lock, N., Dippel, A.-C. & Iversen, B. B. (2014). *Acta Cryst.* A**70**, 39–48.

Blaha, P., Schwarz, K., Madsen, G. K. H., Kvasnicka, D. & Luitz, J. (2008). *WIEN2k – an augmented plane wave and local orbitals program for calculating crystal properties.* Vienna University of Technology, Vienna.

Coppens, P. (1997). *X-ray Charge Densities and Chemical Bonding.* Oxford University Press.

Cummings, S. & Hart, M. (1988). *Aust. J. Phys.* **41**, 423–432.

Dawson, B. (1967). *Proc. R. Soc. A Math. Phys. Eng. Sci.* **298**, 255–263.

Deutsch, M. (1992). *Phys. Rev. B*, **45**, 646–657.

Deutsch, M. & Hart, M. (1988). *Phys. Rev. B*, **37**, 2701–2703.

De Wolff, P. M. (1959). *Appl. Sci. Res.* **7**, 102–112.

Dippel, A.-C., Bindzus, N., Saha, D., Delitz, J. T., Liermann, H.-P., Wahlberg, N., Becker, J., Bøjesen, E. D. & Brummerstedt Iversen, B. (2014). *Z. Anorg. Allg. Chem.* **640**, 3094–3099.

Fischer, A., Tiana, D., Scherer, W., Batke, K., Eickerling, G., Svendsen, H., Bindzus, N. & Iversen, B. B. (2011). *J. Phys. Chem. A*, **115**, 13061–13071.

Flensburg, C. & Stewart, R. F. (1999). *Phys. Rev. B*, **60**, 284–291.

Fujimoto, I. (1974). *Phys. Rev. B*, **9**, 591–599.

Gatti, C. (2005). *Z. Kristallogr.* **220**, 399–457.

Giacovazzo, G. (2002). *Fundamentals of Crystallography*, 2nd ed. Oxford University Press.

Hansen, N. K. & Coppens, P. (1978). *Acta Cryst.* A**34**, 909–921.

Ida, T. (2011). *J. Appl. Cryst.* **44**, 911–920.

Ida, T. & Izumi, F. (2011). *J. Appl. Cryst.* **44**, 921–927.

Johnson, C. K. & Levy, H. A. (1974). *Thermal Motion Analysis Using Bragg Data*. Birmingham: Kynoch Press.

Jørgensen, M. R. V., Hathwar, V. R., Bindzus, N., Wahlberg, N., Chen, Y.-S., Overgaard, J. & Iversen, B. B. (2014). *IUCrJ*, **1**, 267–280.

Kato, N. (1988). *Aust. J. Phys.* **41**, 337–350.

Keating, D., Nunes, A., Batterman, B. & Hastings, J. (1971). *Phys. Rev. B*, **4**, 2472–2478.

Lu, Z. W. & Zunger, A. (1992). *Acta Cryst.* A**48**, 545–554.

Lu, Z. W., Zunger, A. & Deutsch, M. (1993). *Phys. Rev. B*, **47**, 9385–9410.

Nishibori, E., Sunaoshi, E., Yoshida, A., Aoyagi, S., Kato, K., Takata, M. & Sakata, M. (2007). *Acta Cryst.* A**63**, 43–52.

Perdew, J. P., Burke, K. & Ernzerhof, M. (1996). *Phys. Rev. Lett.* **77**, 3865–3868.

Petříček, V., Dušek, M. & Palatinus, L. (2006). *Jana2006 – the crystallographic computing system.* Institute of Physics, Prague, Czech Republic.

Pisani, C., Dovesi, R. & Orlando, R. (1992). *Int. J. Quantum Chem.* **42**, 5–33.

Price, P. F., Maslen, E. N. & Mair, S. L. (1978). *Acta Cryst.* A**34**, 183–193.

Rietveld, H. M. (1969). *J. Appl. Cryst.* **2**, 65–71.

Roberto, J. B. & Batterman, B. W. (1970). *Phys. Rev. B*, **2**, 3220–3226.

Roberto, J. B., Batterman, B. W. & Keating, D. T. (1974). *Phys. Rev. B*, **9**, 2590–2599.

Saka, T. & Kato, N. (1986). *Acta Cryst.* A**42**, 469–478.

Scheringer, C. (1980). *Acta Cryst.* A**36**, 205–210.

Spackman, M. A. (1986). *Acta Cryst.* A**42**, 271–281.

Stewart, R. F. (1976). *Acta Cryst.* A**32**, 565–574.

Straasø, T., Becker, J., Iversen, B. B. & Als-Nielsen, J. (2013). *J. Synchrotron Rad.* **20**, 98–104.

Straasø, T., Dippel, A.-C., Becker, J. & Als-Nielsen, J. (2014). *J. Synchrotron Rad.* **21**, 119–126.

Teworte, R. & Bonse, U. (1984). *Phys. Rev. B*, **29**, 2102–2108.

Trucano, P. & Batterman, B. W. (1972). *Phys. Rev. B*, **6**, 3659–3666.

Wahlberg, N., Bindzus, N., Bjerg, L., Becker, J., Christensen, S., Dippel, A.-C., Jørgensen, M. R. V. & Iversen, B. B. (2015). *J. Phys. Chem. C*, **119**, 6164–6173.

Wilson, A. J. C. (1942). *Nature (London)*, **150**, 151–152.

Yamamoto, K., Takahashi, Y., Ohshima, K., Okamura, F. P. & Yukino, K. (1996). *Acta Cryst.* A**52**, 606–613.

Yang, Y. W. & Coppens, P. (1974). *Solid State Commun.* **15**, 1555–1559.

Zuo, J. M., Blaha, P. & Schwarz, K. (1997). *J. Phys. Condens. Matter*, **9**, 7541–7561.